



Depth-targeted energy delivery deep inside scattering media

Nicholas Bender¹, Alexey Yamilov², Arthur Goetschy³, Hasan Yilmaz^{1,4}, Chia Wei Hsu⁵ and Hui Cao¹

Diffusion makes it difficult to predict and control wave transport through a medium. Overcoming wave diffusion to deliver energy into a target region deep inside a diffusive system is an important challenge for applications, but also represents an interesting fundamental question. It is known that coherently controlling the incident wavefront allows diffraction-limited focusing inside a diffusive system, but in many applications, the targets are significantly larger than a focus and the maximum deliverable energy remains unknown. Here we introduce the 'deposition matrix', which maps an input wavefront to the internal field distribution, and we theoretically predict the ultimate limit on energy enhancement at any depth. Additionally, we find that the maximum obtainable energy enhancement occurs at three-fourths the thickness of the diffusive system, regardless of its scattering strength. We experimentally verify our predictions by measuring the deposition matrix in two-dimensional diffusive waveguides. The experiment gives direct access to the internal field distribution from the third dimension, and we can excite the eigenstates to enhance or suppress the energy within an extended target region. Our analysis reveals that such enhancement or suppression results from both selective transmission-eigenchannel excitation and constructive or destructive interference among these channels.

Depositing energy into a target region deep inside an opaque system—by controlling random wave scattering—is essential in a wide range of applications involving light, microwaves and acoustic waves^{1,2}: for example, deep-tissue imaging^{3,4}, optogenetically controlling neurons^{5,6}, non-invasive ultrasound surgery⁷ and optimization of photoelectrochemical processes in strongly scattering systems⁸. The fundamental challenge to overcome in disordered systems is the multiple scattering of waves, which results in a diffusive spread of wave energy. Controlling the incident wavefront of a coherent beam enables the suppression of wave diffusion, which has been used to focus light to a diffraction-limited spot either inside or through a scattering medium^{9–15}. In many applications, however, targets such as neurons or early-stage tumours are much larger than a wavelength-scaled focal spot, and therefore, the maximum energy that can be delivered to an extended target by shaping the incident wavefront is not known. Experimental investigations have also been hindered by the technical difficulties of finding the optimal input wavefront of a laser beam for maximizing energy delivery. Time-reversal and phase conjugation techniques, which have been employed for focusing to a point¹⁶, cannot provide the optimal input wavefront for an extended region because the final spatial field distribution (speckle pattern) inside the region is not known a priori. Although feedback-based iterative optimization of an input wavefront¹⁵ is efficient at reaching the global maximum for focusing light to a point¹⁷, this is not the case for an extended target¹⁸. Consequently, the physical mechanisms for controlling energy deposition inside diffusive systems as well as the upper bound of energy enhancement remain unclear.

Over the years, various operators and matrices related to physical quantities of interest in disordered systems have been introduced—and their eigenstates studied—in search for the global

optima of quantities. Examples include the field transmission matrix^{18–28}, the energy density matrix²⁹, the photoacoustic transmission matrix³⁰, the generalized Wigner–Smith operator^{31,32}, the time-gated reflection matrix^{33,34}, the acousto-optic transmission matrix³⁵, the dwell-time operator³⁶, the distortion matrix^{37,38} and the Fisher information operator³⁹. None of them, however, provide the solution for maximal energy deposition in an arbitrary-sized region at an arbitrary depth in a scattering medium. More importantly, a general framework for predicting and understanding the ultimate limit on targeted energy delivery into a diffusive system is missing. As such, the following questions are scientifically and technologically important: ‘what are the physical mechanisms contributing to energy deposition, across an extended target, inside a diffusive system?’ and ‘what is the fundamental limit of energy enhancement using a wavefront-control method?’

In this work, we answer these questions by performing a comprehensive experimental, numerical and theoretical study. First, we define the deposition matrix \mathcal{Z} that relates input waves to the corresponding regional field distributions at an arbitrary depth within a diffusive system. The largest eigenvalue of $\mathcal{Z}^\dagger \mathcal{Z}$ gives the maximal energy that can be delivered into the designated region, and the associated eigenvector provides the input wavefront. Next, we build a theoretical model that can analytically predict the probability density function (PDF) of the eigenvalues of $\mathcal{Z}^\dagger \mathcal{Z}$, and demonstrate how energy enhancement depends on the depth of the region and system parameters such as the transport mean free path ℓ and sample thickness L . Although the largest possible energy enhancement scales as L/ℓ , it always occurs at a depth of $(3/4)L$ in a lossless diffusive medium, independent of the scattering strength. Using a unique on-chip disordered-waveguide platform with an interferometric wavefront-shaping setup, experimentally, we use measurements

¹Department of Applied Physics, Yale University, New Haven, CT, USA. ²Physics Department, Missouri University of Science and Technology, Rolla, MO, USA. ³ESPCI Paris, PSL University, CNRS, Institut Langevin, Paris, France. ⁴Institute of Materials Science and Nanotechnology, National Nanotechnology Research Center (UNAM), Bilkent University, Ankara, Turkey. ⁵Ming Hsieh Department of Electrical and Computer Engineering, University of Southern California, Los Angeles, CA, USA. ✉e-mail: yamilov@mst.edu; hui.cao@yale.edu

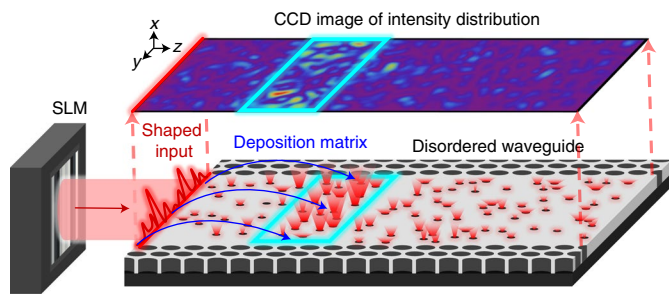


Fig. 1 | Schematic of the experimental platform for investigating energy deposition in a diffusive system. A SLM shapes the 1D incident wavefront of a monochromatic laser beam, and the field distribution inside a 2D disordered waveguide is probed from above. This setup allows the measurement of the deposition matrix that relates the incoming field pattern to the spatial field distribution inside a target region (marked by the cyan box). The selective coupling of light into the deposition eigenchannels can enhance or suppress energy inside the target region, as confirmed by the image (from the CCD camera) of the spatial intensity distribution.

of the internal field distribution to construct the deposition matrix \mathcal{Z} for regions at different depths inside a diffusive system. We then directly excite the individual eigenstates and observe their spatial structures across the entire system. Furthermore, we explore the relationship between deposition and transmission eigenchannels, revealing that regional energy enhancement results from both selective excitation of high-transmission eigenchannels and constructive interference between them.

Experimental platform and deposition matrix

A schematic of our experimental setup for investigating energy deposition in a diffusive system is presented in Fig. 1. We fabricate two-dimensional (2D) disordered structures so that we can probe the field anywhere inside the system from the third dimension, namely, the top. We shape, in one dimension (1D), the incident wavefront of a laser beam using a spatial light modulator (SLM), and extract the 2D field distribution inside the diffusive system with an interferometric measurement. Our planar samples are optical waveguides engraved into a silicon-on-insulator wafer²⁷. Light is confined inside the waveguides by reflective photonic-crystal sidewalls. Randomly distributed air holes are etched throughout a designated region in each waveguide to create optical scattering. Light undergoes multiple scattering and diffusive transport within this disordered region because it is much longer than the transport mean free path ℓ of the scatterers. A small amount of light is scattered out of plane from the holes and interferes with a reference beam. The interference patterns are recorded by a charge-coupled device (CCD) camera, from which the associated field distributions are extracted. Our experimental platform allows the direct mapping of the incident field to the internal fields at any depth.

Controlling energy delivery inside a disordered system requires introducing the deposition matrix \mathcal{Z} for a target region that can have an arbitrary size, shape and depth. The matrix relates an orthonormal set of input wavefronts to the corresponding spatial field distributions within the target region. For instance, we use the lead (empty) waveguide-mode basis to describe the input wavefronts. When light is launched with unit flux into the n th waveguide mode, it impinges on the diffusive region and generates an internal field distribution $E_n(y, z)$. By sampling $E_n(y, z)$ within a target region, the deposition matrix elements are

$$\mathcal{Z}_{mn} \equiv [\epsilon(y_m, z_m)A/M]^{1/2} E_n(y_m, z_m), \quad (1)$$

where A is the area of the target region, which is uniformly sampled by M points; the location of the m th sampling point is given by (y_m, z_m) ; and ϵ is the dielectric constant. The eigenvalues ζ of $\mathcal{Z}^\dagger \mathcal{Z}$ give the total energy inside the target region when sending the corresponding eigenvectors into the system. Therefore, the eigenvector with the highest eigenvalue provides the input wavefront that deposits the most energy into the target region.

As an example case, consider a target region that is a thin slice across the inside of the disordered waveguide, located at depth z_D (Fig. 2a, inset). The slice is so thin that the field variation along the waveguide axis (z axis) is negligible, and only the field distribution along the waveguide cross section (y axis) needs to be sampled. This is done with $M \geq 2N$ evenly spaced points across the waveguide width W , where N is the number of waveguide modes. The sampled field is $E_n(y_m, z_D)$, where m is the index of the sampling point. By representing the internal field E_n in the waveguide-mode basis and ignoring the evanescent waves, we provide a second definition for the deposition matrix in terms of flux:

$$\mathcal{Z}_{mn}(z_D) = \sqrt{v_m} \int_0^W \chi_m^*(y) E_n(y, z_D) dy, \quad (2)$$

where $\chi_m(y)$ is the normalized transverse profile of the m th mode in a homogeneous waveguide with an effective dielectric constant equal to the spatial average of ϵ over the disordered region, and v_m is the propagation speed of the m th mode. In this form, the deposition matrix naturally reduces to the transmission matrix at the end of the disordered region $z_D = L$. For thin slices in our disordered waveguides, the deposition matrices, defined by equations (1) and (2), have nearly identical eigenvalues, and the depth profiles (cross-section-integrated intensity as a function of depth) of the eigenvectors are similar for most slice depths z_D , except when very close to the exit surface $z_D = L$. More details are given in Supplementary Section 1.

Numerical simulation and analytical model

To reveal the full potential of the deposition matrix for energy deposition inside disordered systems, we first carry out numerical simulations of wave propagation in 2D disordered waveguides using the Kwant software package⁴⁰ (Supplementary Section 1.1). For comparison with the transmission matrix, we adopt the deposition matrix defined by equation (2) and calculate its eigenvalues ζ for a thin slice at different depths z_D inside a lossless disordered waveguide. The PDF $P(\zeta)$ (Fig. 2a) is very different from the celebrated bimodal PDF of transmission eigenvalues $P(\tau)$ (ref. 41). At depths $z_D < L$, $P(\zeta)$ has a single peak at $\zeta = 0$, but it develops a second peak at $\zeta = 1$ near the exit surface, that is, $L - z_D < \ell$ (shaded area). We normalize the eigenvalues ζ by their mean $\langle \zeta \rangle$, which represents the typical energy within the slice at depth z_D under random illumination conditions. Despite the lack of a peak at the maximum eigenvalue ζ_{\max} , for most depths, $P(\zeta/\langle \zeta \rangle)$ has a long tail extending beyond the range of $P(\tau/\langle \tau \rangle)$. Consequently, the maximal enhancement of energy inside the diffusive system, given by $\zeta_{\max}/\langle \zeta \rangle$, is larger than the maximum enhancement of transmission $\tau_{\max}/\langle \tau \rangle$ for open channels ($\tau_{\max} = 1$; $\langle \tau \rangle \approx \ell/L \ll 1$). The qualitative difference between $P(\zeta)$ and $P(\tau)$ can be intuitively understood as follows. Due to flux conservation, the transmission eigenvalues are confined to the range $[0, 1]$, and their repulsion makes $P(\tau)$ peak at two boundaries, namely, 0 and 1 (ref. 41). In contrast, there is no upper bound—only a lower bound—for deposition eigenvalues; their repulsion leads a single peak of $P(\zeta)$ at 0 and a tail at large ζ .

To quantitatively interpret these results, we develop an analytical model for the PDF of the deposition eigenvalues $P(\zeta)$. The deposition matrix $\mathcal{Z}(z_D)$ cannot be treated as a random matrix with uncorrelated matrix elements, because the eigenvalue PDF (Fig. 2a) drastically differs from the Marchenko–Pastur law⁴². In particular, the latter predicts that $\langle \zeta_{\max} \rangle / \langle \zeta \rangle = 4$, whereas notably larger values

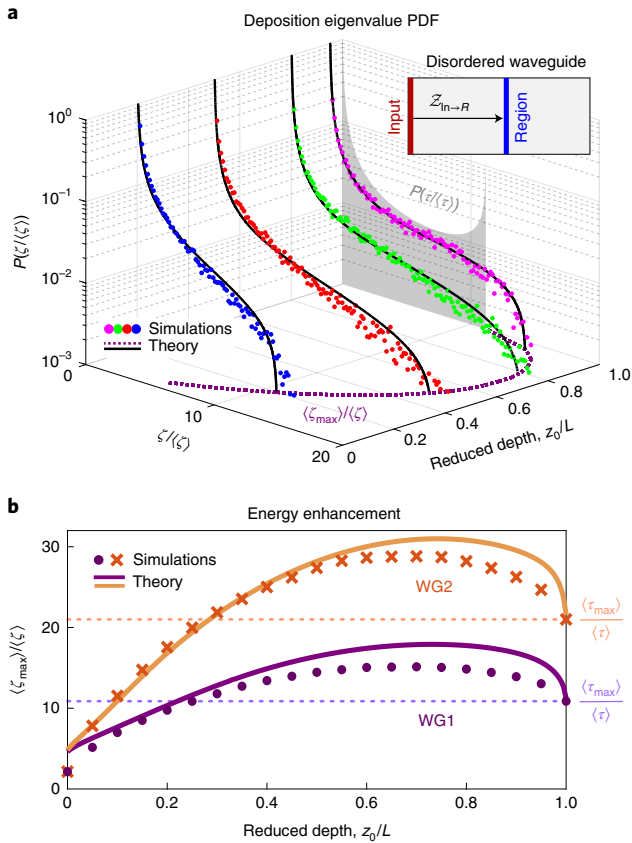


Fig. 2 | Numerical simulation and analytic prediction of deposition eigenvalues. **a**, PDF of normalized deposition eigenvalues $\zeta/\langle\zeta\rangle$ for a thin slice at varying depths z_D inside a diffusive waveguide (inset). Analytical FRM predictions (solid lines) agree with numerical simulations (dots) averaged over 1,000 disorder configurations. For most depths, $P(\zeta/\langle\zeta\rangle)$ is very different from the bimodal distribution of the transmission eigenvalues $P(\tau/\langle\tau\rangle)$, although it converges to bimodal at the end (shaded area at $z_D/L=1$). The theoretical prediction for the upper edge of $P(\zeta/\langle\zeta\rangle)$, which sets the limit for energy enhancement $\langle\zeta_{\max}\rangle/\langle\zeta\rangle$, is marked by the dashed purple line in the horizontal plane. **b**, Energy enhancement in two diffusive waveguides (WG1 and WG2), given by the ratio of the largest ensemble-averaged deposition eigenvalue $\langle\zeta_{\max}\rangle$ over the mean eigenvalue $\langle\zeta\rangle$, increases with depth z_D and reaches its maximum at $z_D/L \approx 3/4$. Analytical predictions for the upper edge of $P(\zeta/\langle\zeta\rangle)$ (solid lines) are compared with the numerical data (symbols). The energy enhancement $\langle\tau_{\max}\rangle/\langle\tau\rangle$ exceeds the transmission enhancement $\langle\zeta_{\max}\rangle/\langle\zeta\rangle$ (horizontal dotted line) at most depths. In **a**, WG1 has length $L=50.0\ \mu\text{m}$, width $W=15.0\ \mu\text{m}$ and transport mean free path $\ell=3.3\ \mu\text{m}$. These values for WG2 in **b** are $L=50.0\ \mu\text{m}$, $W=30.0\ \mu\text{m}$ and $\ell=1.6\ \mu\text{m}$.

are obtained at almost all the depths, indicating that correlations between the elements of $\mathcal{Z}(z_D)$ are beneficial for energy deposition. Since the deposition matrix and transmission matrix coincide at the exit, we build a model that captures the continuous evolution from $P(\zeta)$ at $z_D < L$ to the bimodal PDF at $z_D = L$. This is realized by using a filtered random matrix (FRM) ensemble as initially introduced in ref. ⁴³. This theory amounts to assuming that $\mathcal{Z}(z_D)$ has the same spectrum as a filtered matrix drawn from a larger virtual transmission matrix (Supplementary Section 2). The advantage of this approach is that the full PDF $P(\zeta)$ can be inferred from the first two moments, namely, $\langle\zeta\rangle$ and $\langle\zeta^2\rangle$. We use the numerical values of these two moments as input parameters of the model shown in Fig. 2a. The good agreement between the numerical PDF and the FRM prediction validates our ansatz.

Combining the FRM model with analytical predictions for the first two moments of $P(\zeta)$ (Supplementary Section 2.2), we get theoretical expressions for the full PDF as well as the maximal enhancement. The first moment linearly decays with depth, that is, $\langle\zeta(z_D)\rangle \simeq 2(1-\langle\tau\rangle)(1-z_D/L) + \langle\tau\rangle$, as given by diffusion theory⁴⁴. The second moment is given by the variance $\text{Var}[\zeta(z_D)]$, which is related to the fluctuation of the cross-section-integrated intensity at depth z_D generated by random wavefront illumination²³: $\text{Var}[\zeta(z_D)] \simeq \langle\zeta\rangle^2[1 + NC_2(z_D)]$. In this expression, N is the number of waveguide modes in the disordered region and $C_2(z_D)$ stands for long-range contributions to the spatial intensity correlation function, whose analytical expressions are given in refs. ^{45,46} and Supplementary Section 2.2. Combining these with the FRM model, in the limit $N \gg 1$, we predict a finite support for $P(\zeta)$ and thus a maximal energy enhancement given by the upper edge of $P(\zeta)$. Figure 2b shows a quantitative agreement between this prediction and $\langle\zeta_{\max}\rangle/\langle\zeta\rangle$ evaluated numerically for disordered waveguides of different sizes and scattering strengths, without any adjustable parameter. The FRM model predicts that $\langle\zeta_{\max}\rangle/\langle\zeta\rangle$ only depends on $C_2(z_D)$ for most values of z_D , confirming the crucial role of mesoscopic correlations in enhancing energy deposition. The general expression for energy enhancement is derived and presented in Supplementary Section 2; below, we present a simplified form in the limit of $L \gg \ell$:

$$\frac{\langle\zeta_{\max}(z_D)\rangle}{\langle\zeta(z_D)\rangle} \simeq \frac{3N C_2(z_D)}{2} \simeq \frac{3(z_D/L) - 2(z_D/L)^2}{\langle\tau\rangle}. \quad (3)$$

Two conclusions can be drawn from this result. First, the maximal energy enhancement is inversely proportional to $\langle\tau\rangle$ and thus linearly grows with L/ℓ . In particular, it is independent of the width W of the disordered waveguide as long as the dimensionless conductance $g=N\langle\tau\rangle$ is sufficiently large. Second, apart from $\langle\tau\rangle$, energy enhancement only depends on the reduced depth z_D/L , reaching a maximal value of $9/(8\langle\tau\rangle) \simeq (9/4\pi)(L/\ell)$, in the asymptotic limit of $L/\ell \gg 1$, at $z_D^{(\max)}/L \simeq 3/4$. For moderate values of L/ℓ , the maximum value is larger, but it is still reached at the same depth. This result holds for different transport mean free paths, as shown in Fig. 2b. Hence, the largest enhancement is obtained neither at the output surface ($z_D=L$) nor in the middle of the diffusive medium ($z_D=L/2$), but it is rather achieved at the depth of $(3/4)L$. This result is generic and independent of ℓ . This can be understood from the depth dependence of the long-range correlations created by the interference of scattered waves whose paths are crossed. As the probability of path crossing increases with depth, C_2 grows and reaches its maximum at the depth of $(3/4)L$ (ref. ⁴⁶). The slight decrease in C_2 near the output end is attributed to the increasing possibility of light escaping through the boundary, which reduces wave interference effects.

Measurement of deposition eigenchannels

We experimentally measure different deposition matrices in disordered waveguides like the one shown in Fig. 3a. The disordered region of each waveguide has dimensions of $L=50\ \mu\text{m}$ and $W=15\ \mu\text{m}$. The transport mean free path at the optical wavelength $\lambda=1.55\ \mu\text{m}$ is $\ell=3.20\ \mu\text{m}$. The out-of-plane scattering loss is not negligible; however, as discussed in ref. ⁴⁷, it can be modelled through an effective diffusive dissipation length $\xi_a=28\ \mu\text{m}$. We construct the deposition matrices associated with four target regions inside the disordered waveguide: each is $10\ \mu\text{m} \times 10\ \mu\text{m}$. They are centred at depths $z_D=10, 20, 30$ and $40\ \mu\text{m}$.

We use a SLM to modulate the monochromatic laser beam incident on the waveguide, and measure the field distribution within each target region (Supplementary Section 3). From the data, we extract the deposition matrix and perform a singular value decomposition to obtain the input vectors of the deposition eigenchannels.

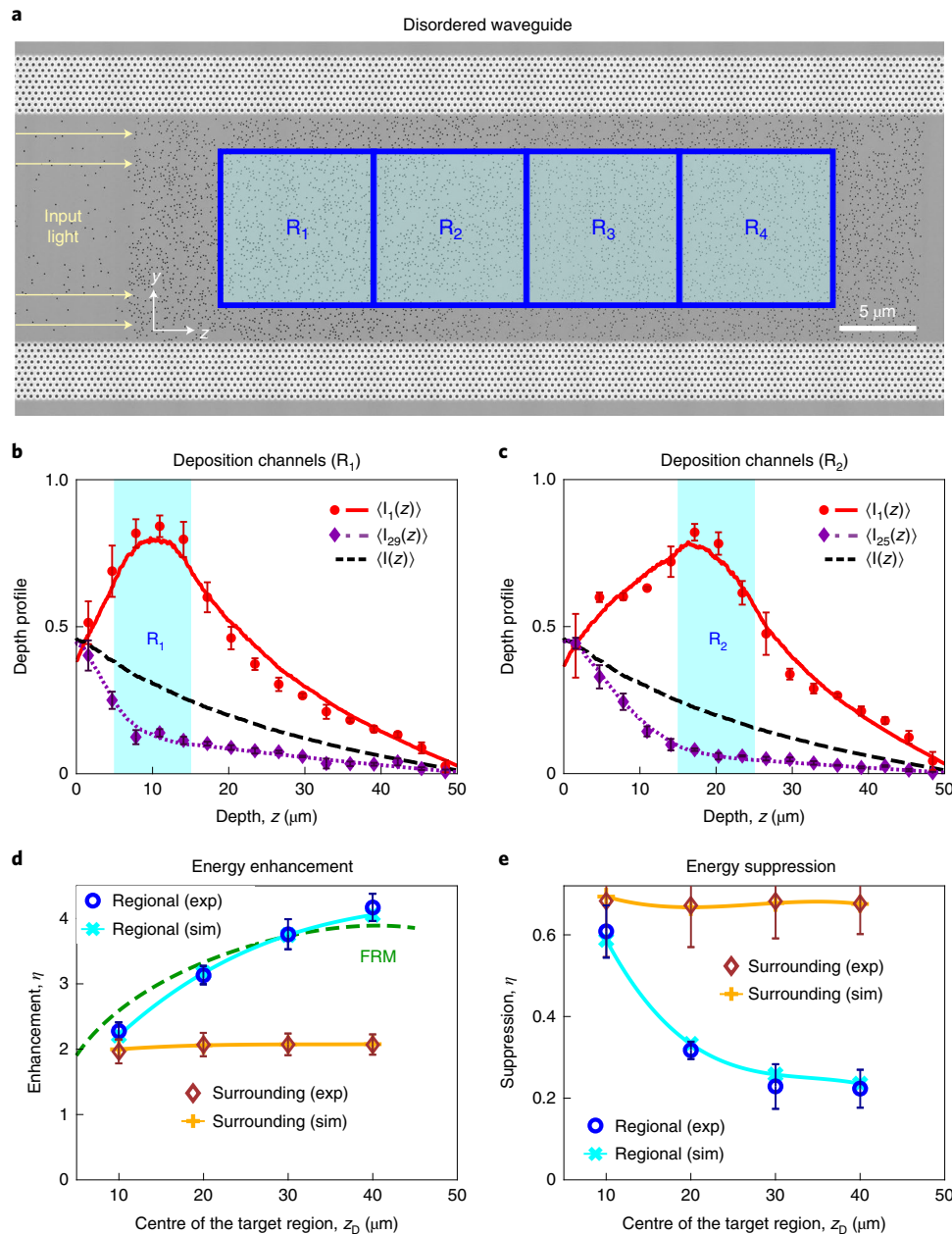


Fig. 3 | Experimental measurement of deposition eigenchannels. **a**, A composite scanning electron microscopy image of a disordered waveguide with width $W=15\ \mu\text{m}$. Randomly distributed air holes (each with a diameter of $100\ \text{nm}$) are etched throughout a designated $50\text{-}\mu\text{m}$ -long region. The four target regions used for energy deposition are superimposed; each is $10\ \mu\text{m} \times 10\ \mu\text{m}$. **b,c**, Depth profiles (cross-section-integrated intensities) of two deposition eigenchannels with enhanced and suppressed energies in target region R_1 centred at depth $z_D=10\ \mu\text{m}$ (**b**) and R_2 at $z_D=20\ \mu\text{m}$ (**c**). The experimentally obtained data for the cross-section-integrated intensity (red circle and purple diamond) agrees with the numerical simulations (red solid line and purple dotted line), and the normalized root-mean-square difference values between the measured and simulated eigenchannels are as follows: 0.10 for $\alpha=1$ and 0.13 for $\alpha=29$ (**b**); 0.08 for $\alpha=1$ and 0.09 for $\alpha=25$ (**c**). The black dashed line is the intensity profile averaged over random input wavefronts. Each experimental data point is averaged over $\Delta z=\ell$, and the error bar corresponds to \pm one standard deviation. **d,e**, Experimentally measured energy enhancement in the target region η_t (blue circles) and surrounding area η_s (brown diamonds) of two deposition eigenchannels $\alpha=2$ (**d**) and $\alpha=24$ (**e**) are compared with the numerical data (light-blue and orange lines; denoted as ‘sim’) for the case of energy deposition into the four target regions centred at $10, 20, 30$ and $40\ \mu\text{m}$. The theoretically predicted maximum energy enhancement, including loss and incomplete channel control (green dashed line in **d**), agrees with the experimental (exp)/numerical results, confirming the essential contribution of long-range intensity correlations to energy deposition.

These vectors are the eigenvectors of $\mathcal{Z}^\dagger \mathcal{Z}$; each is sorted by its corresponding eigenvalue, from high to low, and labelled by index α . We sequentially shape the incident wavefront into each of the eigenvectors, thereby exciting one eigenchannel at a time, and we record the 2D intensity distribution over the entire disordered waveguide. The cross-section-integrated intensity $I_\alpha^{(D)}(z)$ depicts the depth profile

of every eigenchannel. We repeat this measurement for 13 disorder realizations—generated at multiple wavelengths and with different hole configurations—and ensemble average the spatial profiles of the eigenchannels with the same index α (Supplementary Section 3.4). When the average energy density—within the target region—of a measured eigenchannel surpasses that of a random input (with

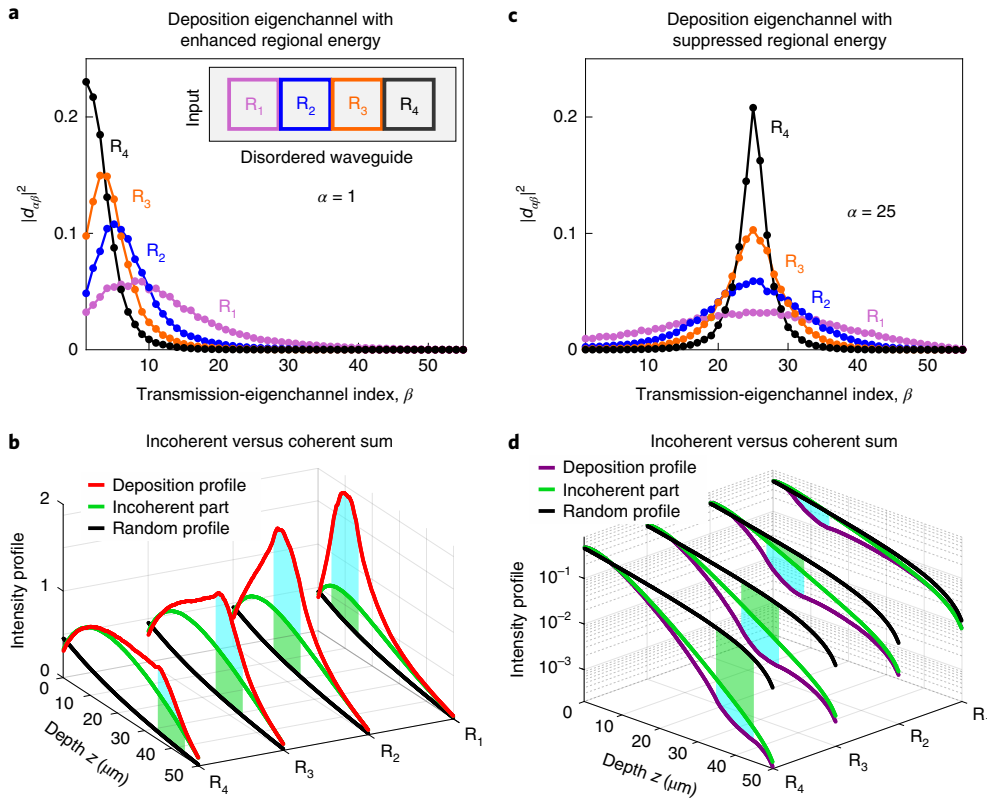


Fig. 4 | Relation between deposition and transmission eigenchannels. **a, c**, Projection of a deposition eigenchannel with index $\alpha=1$ (**a**) or $\alpha=25$ (**c**) onto transmission eigenchannels with index β gives the coefficients d_{app} . Four curves denote $|d_{app}|^2$ for four target regions R_1 – R_4 (inset of **a**) in the same disordered waveguide as in Fig. 3. **b, d**, Comparison of depth profiles between the coherent (red/purple) and incoherent (green) sums of the transmission eigenchannels with coefficients given in **a** (**b**) and **c** (**d**). Although the coherent sum reproduces the deposition-eigenchannel profile, the incoherent sum falls short, and their difference is attributed to interference between the transmission eigenchannels. For each deposition region, enhancement/suppression above/below the random input intensity profile (black solid line) has two distinct contributions from the selective excitation of transmission eigenchannels (green areas) and constructive/destructive interference between them (cyan areas).

an equivalent input flux), we classify it as ‘enhancing’. When the opposite is true, we classify it as ‘suppressing’. For low-indexed (high-indexed) eigenchannels with large (small) eigenvalues, the average energy density inside the target region is enhanced (suppressed); meanwhile, the total reflection decreases (increases) and the total transmission increases (decreases).

In Fig. 3b,c, we show the depth profiles of example eigenchannels with enhanced or suppressed energy deposition for two different target regions. Both strong energy enhancement and suppression are experimentally observed in the target region—when compared with the average depth profile $\langle I(z) \rangle$ of random illumination patterns—and numerically reproduced. Simultaneously, the energy outside the target region is enhanced or suppressed, reflecting the non-local effects in the energy deposition. Quantitatively, we compute the energy enhancement factor in the target region as $\eta_t = \int_{z \in R} I_\alpha(z) dz / \int_{z \in R} \langle I(z) \rangle dz$ and in the surrounding area as $\eta_s = \int_{z \notin R} I_\alpha(z) dz / \int_{z \notin R} \langle I(z) \rangle dz$. Figure 3d shows that η_t increases with depth z_D , whereas η_s remains nearly constant. We account for the square targets in the diffusive waveguides, the out-of-plane scattering loss, as well as the incomplete channel control due to the phase-only SLM used for wavefront shaping, by generalizing the FRM model (Supplementary Sections 2.4 and 2.5). The depth variation of the maximum energy enhancement $\eta_t(z_D)$ is still captured by the long-range contribution, which is integrated over the target area \mathcal{R} as $C_2(z_D) = \int_{z, z' \in \mathcal{R}} C_2(z, z') dz dz'$, where z_D is the centre depth of the square target and $C_2(z, z')$ is the correlation between the cross-section-integrated intensities at depths z and z' for random

input wavefronts. Thus, $\eta_t \propto L/\ell$ in the limit of $L/\ell \gg 1$ and vanishing loss, consistent with ref. 36. In addition, incomplete channel control reduces the size of the filtered matrix used in the model and therefore leads to a reduction in the achievable energy enhancement^{18,23,43}. Due to the presence of loss in the diffusive waveguide and spatial integration of $C_2(z, z')$, the depth of the maximal energy enhancement—which coincides with the maximum of $C_2(z_D)$ —is slightly shifted from $z_D = (3/4)L$ towards the output end. Figure 3e shows that the suppression of energy within the target region gets stronger for larger depths, but the suppression in the surrounding area is independent of depth.

Two mechanisms for energy deposition

To gain a physical insight into the formation of deposition eigenchannels and how they enhance or suppress energy within local regions inside a diffusive system, we decompose them into the transmission eigenchannels, whose spatial profiles have been extensively studied^{20,25,27,36,48–52}. At the entrance of the system ($z=0$), the transmission eigenvectors form a complete basis, and the input wavefront of a deposition eigenchannel can be expressed as a linear superposition of the transmission eigenchannels. The linear mapping from the incident field to the internal field carries the decomposition to the entire field distribution inside the disordered waveguide: $E_\alpha^{(D)}(y, z) = \sum_{\beta=1}^N d_{\alpha\beta} E_\beta^{(T)}(y, z)$. In this expression, $E_\alpha^{(D)}(y, z)$ ($E_\beta^{(T)}(y, z)$) denotes the field distribution of the α th deposition (β th transmission) eigenchannel; further, N is the number of transmission eigenchannels (equal to the number of

propagating modes in the input waveguide). The depth profile of a deposition channel, given by the cross-section-integrated intensity $I_{\alpha}^{(D)}(z) = \int_0^W |E_{\alpha}^{(D)}(y, z)|^2 dy$, consists of two terms:

$$I_{\alpha}^{(D)}(z) = I_{\alpha}^{(i)}(z) + I_{\alpha}^{(c)}(z) \\ = \sum_{\beta=1}^N |d_{\alpha\beta}|^2 I_{\beta}^{(T)}(z) + \sum_{\beta \neq \beta'} d_{\alpha\beta} d_{\alpha\beta'}^* I_{\beta\beta'}^{(T)}(z). \quad (4)$$

The first term ($I_{\alpha}^{(i)}(z)$) is an incoherent sum of the constituent transmission-eigenchannel depth profiles, $I_{\beta}^{(T)}(z) = \int_0^W |E_{\beta}^{(T)}(y, z)|^2 dy$, as studied elsewhere^{20,25,27,36,48–52}. The second term ($I_{\alpha}^{(c)}(z)$) is the result of interference between different transmission eigenchannels inside the diffusive waveguide, which we observe for the first time. Although the transmission eigenchannels are orthogonal at $z=0$ and $z=L$, this is not the case inside:

$$I_{\beta\beta'}^{(T)}(z) = \int_0^W E_{\beta}^{(T)}(y, z) E_{\beta'}^{(T)*}(y, z) dy \neq 0$$

for $0 < z < L$.

To find how much these two terms contribute to the energy enhancement, we numerically decompose the maximal-energy deposition eigenchannels ($\alpha=1$) for the four target regions inside our disordered waveguide. As shown in Fig. 4a, each is composed of multiple high-transmission eigenchannels (higher transmission corresponds to lower index β). With increasing depth z_D , the number of constituent transmission eigenchannels decreases, and the maximal decomposition coefficient $|d_{\alpha\beta}|^2$ shifts to $\beta=1$ (the highest-transmission eigenchannel). Figure 4b shows the incoherent ($I_1^{(i)}(z)$) and coherent ($I_1^{(c)}(z)$) contributions to energy deposition in the target region. When the target region is located at a shallower depth, more transmission eigenchannels participate in constructing the deposition eigenchannel, and their constructive interference plays an important role in enhancing energy deposition in the target region. As the number of participating transmission eigenchannels becomes progressively smaller with increasing depth, the interference effect is weakened and the incoherent contribution from selective excitation of transmission eigenchannels becomes dominant.

We also investigate the deposition eigenchannels that reduce energy within the target regions. As shown in Fig. 4c, the $\alpha=25$ deposition eigenchannels consists of multiple transmission eigenchannels with indices β close to 25. The suppression of energy within the target region results from the selective excitation of lower-transmission eigenchannels and their destructive interference (Fig. 4d). The deeper the target region, the lower the number of constituent transmission eigenchannels and the weaker their destructive interference effect. Owing to the destructive interference, the total transmitted energy can be greater than the energy inside the target region. Thus, when sending light through a diffusive system, it is possible to avoid certain regions inside.

Discussion and conclusions

In conclusion, we have delineated the fundamental limits on depositing energy into a finite region, located at any depth, inside a diffusive system. In contrast to the bimodal distribution of transmission eigenvalues, the PDF of deposition eigenvalues $P(\zeta)$ has only one peak at $\zeta=0$ and a long tail for most depths: $\zeta/\langle\zeta\rangle \gg 1$. Our theoretical model, based on an FRM ensemble, can analytically predict $P(\zeta)$ for regions anywhere inside a diffusive medium. The long-range correlations present in the intensity of the field, induced by the multiple scattering of light and characterized by $C_2(z_D)$, facilitate optical energy deposition. In a diffusive waveguide of length L much larger than the transport mean free path ℓ , the largest

possible energy enhancement $\langle\zeta_{\max}\rangle/\langle\zeta\rangle$ at depth z_D only depends on two parameters, namely, L/ℓ and z_D/L . With increasing depth z_D , $\langle\zeta_{\max}\rangle/\langle\zeta\rangle$ rises and reaches a global maximum proportional to L/ℓ at $z_D^{(\max)}/L \simeq 3/4$. Because $z_D^{(\max)}$ is dependent on L and independent of ℓ , when $L \gg \ell$, the depth of the maximum enhancement is deep inside the sample rather than near the front or back surfaces. Although our experimental and numerical studies are conducted on 2D systems, the above scaling results follow from the filtered matrix theory, such as equation (3), which also applies in three dimensions.

Additionally, we discovered the relationship between deposition and transmission eigenchannels. We found that it is impossible to construct the intensity profile of a deposition eigenchannel from the intensity profiles of the transmission eigenchannels alone. Constructive or destructive interference between transmission eigenchannels inside the disordered system plays a prominent role in enhancing or suppressing energy within the target region. Therefore, our analysis reveals two distinct mechanisms for energy deposition: selective excitation of transmission eigenchannels and interference between them. Their contributions are characterized by the amplitudes and phases of the coefficients obtained when decomposing a deposition eigenchannel into a summation of transmission eigenchannels.

The universality of the FRM formalism and long-range intensity correlations indicates that our conclusions—drawn from the current studies on planar waveguides with narrow widths and transverse confinement—can be generalized to wide slabs with open boundaries as well as volumetric diffusive systems. They are also applicable to other types of wave such as microwaves and acoustic waves. Targeted energy delivery opens the door to numerous applications, for example, optogenetic control of cells, photothermal therapy, and probing and manipulating photoelectrochemical processes deep inside nominally opaque media. Since short pulses are often used for energy delivery, a future direction is to extend the concept of the deposition matrix to the time domain to utilize the temporal degrees of freedom provided by the diffusive medium. Although the current study is conducted on diffusive systems, our experimental platform and methodology can be employed to investigate deposition eigenchannels in 2D localized samples, where the transport is dominated by the highest-transmission eigenchannel. It may also be used to explore energy deposition inside disordered photonic crystals⁵³ and coupled resonator optical waveguides, which are essential building blocks in on-chip photonic circuits.

Online content

Any methods, additional references, Nature Research reporting summaries, source data, extended data, supplementary information, acknowledgements, peer review information; details of author contributions and competing interests; and statements of data and code availability are available at <https://doi.org/10.1038/s41567-021-01475-x>.

Received: 31 May 2021; Accepted: 23 November 2021;
Published online: 27 January 2022

References

- Mosk, A. P., Lagendijk, A., Lerosey, G. & Fink, M. Controlling waves in space and time for imaging and focusing in complex media. *Nat. Photon.* **6**, 283–292 (2012).
- Rotter, S. & Gigan, S. Light fields in complex media: mesoscopic scattering meets wave control. *Rev. Mod. Phys.* **89**, 015005 (2017).
- Yu, H. et al. Recent advances in wavefront shaping techniques for biomedical applications. *Curr. Appl. Phys.* **15**, 632–641 (2015).
- Yoon, S. et al. Deep optical imaging within complex scattering media. *Nat. Rev. Phys.* **2**, 141–158 (2020).
- Yoon, J. et al. Optogenetic control of cell signaling pathway through scattering skull using wavefront shaping. *Sci. Rep.* **5**, 13289 (2015).
- Ruan, H. et al. Deep tissue optical focusing and optogenetic modulation with time-reversed ultrasonically encoded light. *Sci. Adv.* **3**, eaa05520 (2017).

7. Pernot, M. et al. In vivo transcranial brain surgery with an ultrasonic time reversal mirror. *J. Neurosurg.* **106**, 1061–1066 (2007).
8. Liew, S. F. et al. Coherent control of photocurrent in a strongly scattering photoelectrochemical system. *ACS Photon.* **3**, 449–455 (2016).
9. Vellekoop, I. M. & Mosk, A. Focusing coherent light through opaque strongly scattering media. *Opt. Lett.* **32**, 2309–2311 (2007).
10. Yaqoob, Z., Psaltis, D., Feld, M. S. & Yang, C. Optical phase conjugation for turbidity suppression in biological samples. *Nat. Photon.* **2**, 110–115 (2008).
11. Vellekoop, I. M., Van Putten, E., Lagendijk, A. & Mosk, A. Demixing light paths inside disordered metamaterials. *Opt. Express* **16**, 67–80 (2008).
12. Xu, X., Liu, H. & Wang, L. V. Time-reversed ultrasonically encoded optical focusing into scattering media. *Nat. Photon.* **5**, 154–157 (2011).
13. Judkewitz, B., Wang, Y. M., Horstmeyer, R., Mathy, A. & Yang, C. Speckle-scale focusing in the diffusive regime with time reversal of variance-encoded light (TROVE). *Nat. Photon.* **7**, 300–305 (2013).
14. Horstmeyer, R., Ruan, H. & Yang, C. Guidestar-assisted wavefront-shaping methods for focusing light into biological tissue. *Nat. Photon.* **9**, 563–571 (2015).
15. Vellekoop, I. M. Feedback-based wavefront shaping. *Opt. Express* **23**, 12189–12206 (2015).
16. Fink, M. et al. Time-reversed acoustics. *Rep. Prog. Phys.* **63**, 1933 (2000).
17. Vellekoop, I. M. & Mosk, A. P. Universal optimal transmission of light through disordered materials. *Phys. Rev. Lett.* **101**, 120601 (2008).
18. Hsu, C. W., Liew, S. F., Goetschy, A., Cao, H. & Stone, A. D. Correlation-enhanced control of wave focusing in disordered media. *Nat. Phys.* **13**, 497–502 (2017).
19. Popoff, S. et al. Measuring the transmission matrix in optics: an approach to the study and control of light propagation in disordered media. *Phys. Rev. Lett.* **104**, 100601 (2010).
20. Choi, W., Mosk, A. P., Park, Q.-H. & Choi, W. Transmission eigenchannels in a disordered medium. *Phys. Rev. B* **83**, 134207 (2011).
21. Kim, M. et al. Maximal energy transport through disordered media with the implementation of transmission eigenchannels. *Nat. Photon.* **6**, 581–585 (2012).
22. Yu, H. et al. Measuring large optical transmission matrices of disordered media. *Phys. Rev. Lett.* **111**, 153902 (2013).
23. Popoff, S. M., Goetschy, A., Liew, S. F., Stone, A. D. & Cao, H. Coherent control of total transmission of light through disordered media. *Phys. Rev. Lett.* **112**, 133903 (2014).
24. Gérardin, B., Laurent, J., Derode, A., Prada, C. & Aubry, A. Full transmission and reflection of waves propagating through a maze of disorder. *Phys. Rev. Lett.* **113**, 173901 (2014).
25. Davy, M., Shi, Z., Park, J., Tian, C. & Genack, A. Z. Universal structure of transmission eigenchannels inside opaque media. *Nat. Commun.* **6**, 6893 (2015).
26. Yilmaz, H., Hsu, C. W., Yamilov, A. & Cao, H. Transverse localization of transmission eigenchannels. *Nat. Photon.* **13**, 352–358 (2019).
27. Bender, N., Yamilov, A., Yilmaz, H. & Cao, H. Fluctuations and correlations of transmission eigenchannels in diffusive media. *Phys. Rev. Lett.* **125**, 165901 (2020).
28. Hsu, C. W., Goetschy, A., Bromberg, Y., Stone, A. D. & Cao, H. Broadband coherent enhancement of transmission and absorption in disordered media. *Phys. Rev. Lett.* **115**, 223901 (2015).
29. Cheng, X. & Genack, A. Z. Focusing and energy deposition inside random media. *Opt. Lett.* **39**, 6324–6327 (2014).
30. Chaigne, T. et al. Controlling light in scattering media non-invasively using the photoacoustic transmission matrix. *Nat. Photon.* **8**, 58–64 (2014).
31. Ambichl, P. et al. Focusing inside disordered media with the generalized Wigner-Smith operator. *Phys. Rev. Lett.* **119**, 033903 (2017).
32. Horodyski, M. et al. Optimal wave fields for micromanipulation in complex scattering environments. *Nat. Photon.* **14**, 149–153 (2020).
33. Jeong, S. et al. Focusing of light energy inside a scattering medium by controlling the time-gated multiple light scattering. *Nat. Photon.* **12**, 277–283 (2018).
34. Badon, A. et al. Smart optical coherence tomography for ultra-deep imaging through highly scattering media. *Sci. Adv.* **2**, e1600370 (2016).
35. Katz, O., Ramaz, F., Gigan, S. & Fink, M. Controlling light in complex media beyond the acoustic diffraction-limit using the acousto-optic transmission matrix. *Nat. Commun.* **10**, 717 (2019).
36. Durand, M., Popoff, S. M., Carminati, R. & Goetschy, A. Optimizing light storage in scattering media with the dwell-time operator. *Phys. Rev. Lett.* **123**, 243901 (2019).
37. Lambert, W., Cobus, L. A., Frappart, T., Fink, M. & Aubry, A. Distortion matrix approach for ultrasound imaging of random scattering media. *Proc. Natl Acad. Sci. USA* **117**, 14645–14656 (2020).
38. Badon, A. et al. Distortion matrix concept for deep optical imaging in scattering media. *Sci. Adv.* **6**, eaay7170 (2020).
39. Bouchet, D., Rotter, S. & Mosk, A. P. Maximum information states for coherent scattering measurements. *Nat. Phys.* **17**, 564–568 (2021).
40. Groth, C. W., Wimmer, M., Akhmerov, A. R. & Waintal, X. Kwant: a software package for quantum transport. *New J. Phys.* **16**, 063065 (2014).
41. Beenakker, C. W. Random-matrix theory of quantum transport. *Rev. Mod. Phys.* **69**, 731–808 (1997).
42. Marchenko, V. A. & Pastur, L. A. Distribution of eigenvalues for some sets of random matrices. *Math. USSR Sb.* **1**, 457 (1967).
43. Goetschy, A. & Stone, A. D. Filtering random matrices: the effect of incomplete channel control in multiple scattering. *Phys. Rev. Lett.* **111**, 063901 (2013).
44. van Rossum, M. C. W. & Nieuwenhuizen, T. M. Multiple scattering of classical waves: microscopy, mesoscopy, and diffusion. *Rev. Mod. Phys.* **71**, 313 (1999).
45. Pnini, R. & Shapiro, B. Fluctuations in transmission of waves through disordered slabs. *Phys. Rev. B* **39**, 6986–6994 (1989).
46. Sarma, R., Yamilov, A., Neupane, P., Shapiro, B. & Cao, H. Probing long-range intensity correlations inside disordered photonic nanostructures. *Phys. Rev. B* **90**, 014203 (2014).
47. Yamilov, A. G. et al. Position-dependent diffusion of light in disordered waveguides. *Phys. Rev. Lett.* **112**, 023904 (2014).
48. Sarma, R., Yamilov, A., Petrenko, S., Bromberg, Y. & Cao, H. Control of energy density inside a disordered medium by coupling to open or closed channels. *Phys. Rev. Lett.* **117**, 086803 (2016).
49. Ojambati, O. S., Mosk, A. P., Vellekoop, I. M., Lagendijk, A. & Vos, W. L. Mapping the energy density of shaped waves in scattering media onto a complete set of diffusion modes. *Opt. Express* **24**, 18525–18540 (2016).
50. Koirala, M., Sarma, R., Cao, H. & Yamilov, A. Inverse design of perfectly transmitting eigenchannels in scattering media. *Phys. Rev. B* **96**, 054209 (2017).
51. Hong, P., Ojambati, O. S., Lagendijk, A., Mosk, A. P. & Vos, W. L. Three-dimensional spatially resolved optical energy density enhanced by wavefront shaping. *Optica* **5**, 844–849 (2018).
52. Fang, P. et al. Universality of eigenchannel structures in dimensional crossover. *Phys. Rev. B* **99**, 094202 (2019).
53. Uppu, R., Adhikary, M., Hartevelde, C. A. M. & Vos, W. L. Spatially shaping waves to penetrate deep inside a forbidden gap. *Phys. Rev. Lett.* **126**, 177402 (2021).

Publisher's note Springer Nature remains neutral with regard to jurisdictional claims in published maps and institutional affiliations.

© The Author(s), under exclusive licence to Springer Nature Limited 2022

Methods

Optical setup. A detailed schematic of our experimental setup is presented in the Supplementary Information. A wavelength-tunable laser (Keysight 81960A) outputs a linearly polarized continuous-wave beam with a wavelength of around 1,554 nm. The collimated beam is split into two beams by using a 50/50 beam splitter. One is used as a reference beam, whereas the other illuminates the phase-modulating surface of a phase-only SLM (Hamamatsu LCOS-SLM X10468). A 1D phase-modulation pattern consisting of 128 macropixels is displayed on the SLM. Each micropixel has 4×800 pixels of SLM. We image the field reflected from the SLM plane onto the back focal plane of a long-working-distance objective Obj. 1 (Mitutoyo M Plan Apo NIR HR100 \times with a numerical aperture of 0.7) using two lenses with focal lengths of $f_1 = 400$ mm and $f_2 = 75$ mm. To prevent unmodulated light from entering the objective lens, we display a binary diffraction grating within each macropixel to shift the modulated light away from the unmodulated light in the focal plane of the first lens f_1 . With a slit in the focal plane, we block all the light except the phase-modulated light in the first diffraction order. Right after the slit and before the second lens f_2 , we insert a half-wave ($\lambda/2$) plate to rotate the polarization of light so that it is transverse-electric polarized relative to our waveguide sample. The waveguide entrance at the edge of our silicon-on-insulator wafer is placed at the front focal plane of Obj. 1 so that it is illuminated with the Fourier transform of the phase-modulation pattern displayed on the SLM. From the top of the wafer, another long-working-distance objective (Obj. 2; Mitutoyo M Plan Apo NIR HR100 \times) collects light scattered out of plane from the waveguide. We use a third lens with a focal length of $f_3 = 100$ mm together with Obj. 2 to image the sample. In conjunction, the lens and objective magnify the sample image by 50 times. Using a second beam splitter, we combine the light collected from the sample with the reference beam. Their interference patterns are recorded with an infrared CCD camera (Allied Vision Goldeye G-032 Cool).

Data availability

Source data are available for this paper. All other data that support the plots within this paper and other findings of this study are available from the corresponding authors upon reasonable request.

Acknowledgements

H.C. thanks A. Genack for stimulating discussions. **Funding:** this work is partly supported by the Office of Naval Research (ONR) under grant no. N00014-20-1-2197, and by the National Science Foundation under grant nos. DMR-1905465, DMR-1905442 and OAC-1919789.

Author contributions

N.B. conducted the experiments and analysed the data. A.Y. performed the numerical simulations. A.G. developed the analytical model. H.Y. participated in the experimental study. C.W.H. contributed to the theoretical analysis. H.C. initiated the project and supervised the research. All the authors contributed to manuscript preparation.

Competing interests

The authors declare no competing interests.

Additional information

Supplementary information The online version contains supplementary material available at <https://doi.org/10.1038/s41567-021-01475-x>.

Correspondence and requests for materials should be addressed to Alexey Yamilov or Hui Cao.

Peer review information *Nature Physics* thanks Alexandre Aubry, Oluwafemi Ojambati and Patrick Sebbah for their contribution to the peer review of this work.

Reprints and permissions information is available at www.nature.com/reprints.